Contents lists available at ScienceDirect

Journal of Fluids and Structures

journal homepage: www.elsevier.com/locate/jfs



Circulation dynamics of small-amplitude pitching airfoil undergoing laminar-to-turbulent transition



Amir S. Rezaei *. Haithem Taha

Department of Mechanical and Aerospace Engineering, University of California, Irvine, CA, 92617, USA

ARTICLE INFO

Article history:
Received 16 January 2020
Received in revised form 13 September 2020
Accepted 21 October 2020
Available online xxxx

Keywords:
Circulation dynamics
Kutta condition
Laminar-to-turbulent transition
Computational fluid dynamics
Pitching airfoil
Unsteady aerodynamics

ABSTRACT

This study is motivated by the non-linear behavior of the lift response of a pitching airfoil with a small amplitude and frequency where a linear behavior is expected. The validated $\gamma - Re_{\theta}$ transition model coupled with $k - \omega$ SST (shear stress transport) turbulence model was utilized to solve the unsteady Reynolds-averaged Navier-Stokes (URANS) equations for a harmonically pitching NACA 0012 at Reynolds numbers 75×10^3 , 200×10^3 and reduced frequencies 0.05 - 0.3. First, the numerical setup was validated against experimental results for a pitching airfoil undergoing laminar-to-turbulent transition. Then, the circulation dynamics were investigated following an exact derivation of the Kutta condition. Unlike the classical Kutta condition which assumes a vanishing pressure loading at the sharp trailing-edge, it is shown that the transition induces non-linearity in the lift dynamics by creating a significant pressure variation across the boundary layer in the vicinity of the trailing-edge, affecting the development of the bound circulation around the airfoil. Moreover, the effects of reduced frequency, pitching amplitude and Reynolds number on the circulation dynamics were studied in both frequency and time domains. The results shed light on the further enhancement of potential flow-based solutions to capture non-linearity in the lift dynamics due to transition.

© 2020 Elsevier Ltd. All rights reserved.

1. Introduction

There are many recent applications in aeronautical engineering that operate in the low-to-moderate Reynolds number regime, such as high-altitude flying ships (Greer et al., 2000) or unmanned-aerial-vehicles and micro-air-vehicles (Mueller and DeLaurier, 2003; Elsadek et al., 2017). These vehicles typically operate at low speeds and possess short characteristic length scales, necessitating more research to obtain a deeper understanding of the low-to-moderate Reynolds number aerodynamics for various configurations. The corresponding Reynolds number for these applications ranges from $10^4 - 10^5$, at which laminar-to-turbulent transition is prone to happen (Pelletier and Mueller, 2000; McMasters and Henderson, 1980).

In the literature, transition has been mostly studied in dynamic stall where the airfoil experiences large deflections (Lee and Gerontakos, 2004; Gupta and Ansell, 2018; Benton and Visbal, 2019; Deparday and Mulleners, 2019). However, the cases with small deflections drew less attention in the literature. The majority of the previous efforts in this direction (McCroskey and Puccif, 1982; Dovgal et al., 1994; Kim and Chang, 2014; Raffel et al., 2015) have investigated the temporal–spatial growth or decay of different types of instabilities and the mechanisms triggering the transition onset, which are enhanced at lower Reynolds numbers. Most of these studies have been mainly concerned with how the

E-mail address: asrezaei@uci.edu (A.S. Rezaei).

^{*} Corresponding author.

bHalf chord $(\frac{c}{2})$ α Geometric angle of attack U_{∞} Free stream velocity U Local velocity ω Pitching motion angular velocity T Pitching motion period $(\frac{2\pi}{\omega})$ k Reduced frequency $(\frac{\omega b}{U_{\infty}})$ A Amplitude of pitching $\dot{\Gamma}$ Rate of changing of the circulation α Geometric angle of attack α_u Angle of attack during upstroke motion α_d Angle of attack during downstroke motion y_{upper} y-coordinate of the boundary layer on the top surface y_{lower} y-coordinate of the boundary layer on the bottom surface Δy Difference in the thickness of the top and bottom boundary layer μ Dynamic viscosity ρ Density Re Chord based Reynolds number	
$\begin{array}{cccccccccccccccccccccccccccccccccccc$	
U Local velocity ω Pitching motion angular velocity T Pitching motion period $(\frac{2\pi}{\omega})$ k Reduced frequency $(\frac{\omega b}{U_{\infty}})$ A Amplitude of pitching $\dot{\Gamma}$ Rate of changing of the circulation α Geometric angle of attack α_u Angle of attack during upstroke motion y_{upper} y-coordinate of the boundary layer on the top surface y_{lower} y-coordinate of the boundary layer on the bottom surface Δy Difference in the thickness of the top and bottom boundary layer μ Dynamic viscosity μ_t Eddy viscosity ρ Density Re Chord based Reynolds number	
$\begin{array}{cccccccccccccccccccccccccccccccccccc$	
TPitching motion period $(\frac{2\pi}{\omega})$ kReduced frequency $(\frac{\omega b}{U_{\infty}})$ AAmplitude of pitching $\dot{\Gamma}$ Rate of changing of the circulation α Geometric angle of attack α_u Angle of attack during upstroke motion α_d Angle of attack during downstroke motion y_{upper} y-coordinate of the boundary layer on the top surface y_{lower} y-coordinate of the boundary layer on the bottom surface Δy Difference in the thickness of the top and bottom boundary layer μ Dynamic viscosity μ_t Eddy viscosity ρ DensityReChord based Reynolds number	
kReduced frequency $(\frac{\omega b}{U_{\infty}})$ AAmplitude of pitching $\dot{\Gamma}$ Rate of changing of the circulation α Geometric angle of attack α_u Angle of attack during upstroke motion α_d Angle of attack during downstroke motion y_{upper} y-coordinate of the boundary layer on the top surface y_{lower} y-coordinate of the boundary layer on the bottom surface Δy Difference in the thickness of the top and bottom boundary layer μ Dynamic viscosity μ_t Eddy viscosity ρ DensityReChord based Reynolds number	
AAmplitude of pitching $\dot{\Gamma}$ Rate of changing of the circulation α Geometric angle of attack α_u Angle of attack during upstroke motion α_d Angle of attack during downstroke motion y_{upper} y-coordinate of the boundary layer on the top surface y_{lower} y-coordinate of the boundary layer on the bottom surface Δy Difference in the thickness of the top and bottom boundary layer μ Dynamic viscosity μ_t Eddy viscosity ρ Density Re Chord based Reynolds number	
AAmplitude of pitching $\dot{\Gamma}$ Rate of changing of the circulation α Geometric angle of attack α_u Angle of attack during upstroke motion α_d Angle of attack during downstroke motion y_{upper} y-coordinate of the boundary layer on the top surface y_{lower} y-coordinate of the boundary layer on the bottom surface Δy Difference in the thickness of the top and bottom boundary layer μ Dynamic viscosity μ_t Eddy viscosity ρ Density Re Chord based Reynolds number	
$lpha$ Geometric angle of attack $lpha_u$ Angle of attack during upstroke motion $lpha_d$ Angle of attack during downstroke motion y_{upper} y-coordinate of the boundary layer on the top surface y_{lower} y-coordinate of the boundary layer on the bottom surface Δy Difference in the thickness of the top and bottom boundary layer μ Dynamic viscosity μ_t Eddy viscosity ρ Density Re Chord based Reynolds number	
$lpha$ Geometric angle of attack $lpha_u$ Angle of attack during upstroke motion $lpha_d$ Angle of attack during downstroke motion y_{upper} y-coordinate of the boundary layer on the top surface y_{lower} y-coordinate of the boundary layer on the bottom surface Δy Difference in the thickness of the top and bottom boundary layer μ Dynamic viscosity μ_t Eddy viscosity ρ Density Re Chord based Reynolds number	
$lpha_d$ Angle of attack during downstroke motion y_{upper} y-coordinate of the boundary layer on the top surface y_{lower} y-coordinate of the boundary layer on the bottom surface Δy Difference in the thickness of the top and bottom boundary layer μ Dynamic viscosity μ_t Eddy viscosity ρ Density Re Chord based Reynolds number	
y_{upper} y-coordinate of the boundary layer on the top surface y_{lower} y-coordinate of the boundary layer on the bottom surface Δy Difference in the thickness of the top and bottom boundary layer μ Dynamic viscosity μ_t Eddy viscosity ρ Density Re Chord based Reynolds number	
y_{lower} y-coordinate of the boundary layer on the bottom surface Δy Difference in the thickness of the top and bottom boundary layer μ Dynamic viscosity μ_t Eddy viscosity ρ Density Re Chord based Reynolds number	
Δy Difference in the thickness of the top and bottom boundary layer μ Dynamic viscosity μ_t Eddy viscosity ρ Density Re Chord based Reynolds number	
μ Dynamic viscosity μ_t Eddy viscosity ρ Density Re Chord based Reynolds number	
μ_t Eddy viscosity $ ho$ Density Re Chord based Reynolds number	
ρ Density Re Chord based Reynolds number	
Re Chord based Reynolds number	
$Re_{ heta}$ Momentum-thickness Reynolds number	
$\hat{Re}_{ heta t}$ Local transition onset momentum-thickness Reynolds number	
heta Momentum thickness	
γ Intermittency	
TI Turbulent intensity	
TE Trailing-edge	

laminar separation bubble (LSB) is formed in transitional flows, which is typically accompanied by laminar-to-turbulent transition (Smith, 1986). Nevertheless, few articles (Lorber and Carta, 1994; Poirel and Mendes, 2014 among others) motivated by the flutter analysis, have studied the effect of transition on aerodynamic loads. The focus of this paper is on the latter study from a new aerodynamics perspective by analyzing the circulation dynamics in transitional flow.

As discussed by Poirel and Mendes (2014) and Negi et al. (2018), transition significantly influences the aerodynamic characteristics of the airfoil by introducing non-linearities in the response. This behavior is also seen in the experimental effort of Kim and Chang (2014) who studied a pitching airfoil at transitional Reynolds numbers $(2 \times 10^4 - 5 \times 10^4)$. Raffel et al. (2015) and Liu et al. (2018) who performed experimental and numerical analysis, respectively, concluded that the transition location of a pitching airfoil possesses a non-trivial frequency response and non-linear behavior can be observed in their results, even under small deflections.

In the past century, most of the efficient unsteady aerodynamics models (Wagner, 1925; Theodorsen and Mutchler, 1935; Darakananda and Eldredge, 2019 among others) were developed by adopting the potential flow setup. In these approaches, the effect of viscosity is taken into account solely through the auxiliary condition at the sharp edges, which determines the rate of vorticity shed from the boundary layer to the wake and dictates the amount of circulation (or lift) on the airfoil (Taha and Rezaei, 2019). If the correct amount of circulation is supplied to the potential flow framework, it is capable of providing reasonable results for the flow field and aerodynamic loads. The most utilized condition is the well-known Kutta condition, which neglects non-linear effects from transition. As a result, the classical models based on potential flow cannot predict transition effects on the resulting aerodynamic loads in the low-to-moderate range of Reynolds numbers. While this fact is well-known to aerodynamicists, what these models exactly lack to better capture transition effects is less known. In other words, how can one augment potential flow models with high-fidelity simulation and/or experimental data to account for transition effects on the lift dynamics in a simple way? The current effort provides an answer to this question.

The objective of this paper is to investigate the non-linear effects of transition on the lift and circulation dynamics of a pitching airfoil at low-to-moderate Reynolds numbers. By deriving the exact version of the hypothesized Kutta condition, we show the contribution of the pressure gradient across the boundary layer in the presence of transition (and LSB), which is neglected in the classical Kutta condition. To this end, the unsteady incompressible Reynolds-averaged Navier–Stokes equations have been numerically solved. The finite-volume computational fluid dynamics (CFD) solver ANSYS Fluent 18.2 has been employed using the $\gamma - Re_{\theta}$ (or transition-SST) closure model by Langtry and Menter (2009), which showed

satisfactory results in transition prediction for aerodynamic applications including complex cases involving dynamic stall (Wang et al., 2010; Gharali and Johnson, 2013). In this study, the considered pitching amplitudes are far below the dynamic stall, and the oscillation reduced frequencies are low. Therefore, the SST transition model is a good candidate for this study. The numerical setup and validation against an experimental study by Kim and Chang (2014) on a pitching airfoil at transitional Reynolds number are explained in Sections 2 and 3, which follows our conference paper (Rezaei and Taha, 2019). Lastly, in Section 4, the effect of different parameters such as Reynolds number, pitching amplitude and reduced frequency on circulation dynamics is studied, and a connection is drawn between transition and the rate of circulation development (equivalently the rate of vorticity shed at the sharp edge). Based on this connection, extension of the classical unsteady approaches can be performed to account for the non-linear lift dynamics in the transition regime by modifying the edge condition (i.e., the Kutta condition).

2. Numerical setup

The farfield unstructured mesh and the conformal grid resolution near the airfoil is shown in Fig. 1. This hybrid mesh comprises a very dense structured mesh near the airfoil, which contains the boundary layer in all the studied cases, followed by an unstructured mesh, which facilitates the dynamic mesh approach. The O-type farfield has been used and divided into three rings where the intermediate ring (red) accommodates the airfoil motion via a dynamic mesh, the inner ring (blue) moves with the airfoil like a rigid body, and the outer ring (green) is fixed. This technique maintains the generated high quality grid near the airfoil described below as no deformation or remeshing occurs in the inner ring. The geometry and methodology are almost identical to that in Taha and Rezaei (2018) except for two changes. The first alteration is adding more layers of grids inside the boundary layer to guarantee that the dimensionless distance $y^+ \equiv \frac{\rho u_r y}{\rho} < 1$ (where $u_\tau = \sqrt{\frac{\tau_w}{\rho}}$ is the friction velocity, $\tau_w = \frac{dU}{dy}|_{y=y_w}$ is the wall shear stress, and y is the distance from

the nearest wall) for all the case studies with 250 grid points on each side of the airfoil. Note that $y^+ < 1$ is required for the grid resolution near the wall since the adopted turbulence model $(k - \omega SST)$ does not utilize wall function, but is valid all the way down to the near-wall region. Therefore, sufficient grid layers near the wall are needed to capture the viscous sublayer, where $y^+ \sim < 5$. Also, a coarser mesh was generated for grid independence study and similar results were observed. However, the denser mesh was chosen for the rest of the study since the computational time was not a big concern and to be conservative. This high grid resolution helps to better capture the events inside the boundary layer and the flow field near the trailing-edge which requires capturing the edge of the boundary layer and finding the vorticity fluxes into the wake as proposed by Sears (1976) and demonstrated below. The high-performance computer (HPC) at the university of California, Irvine, was utilized for all the simulations with 32 CPUs in parallel, where the clock speed of the processors was 2.2 GHz. The total simulation time for running 4 complete pitching cycles of the airfoil was almost 15 h. (For more details about the grid topology, dynamic mesh and solution setup in the solver, the reader is referred to Taha and Rezaei (2018))

The second difference is employing the local correlation-based $\gamma-Re_{\theta}$ transition model (Menter et al., 2006) which is compatible with the unstructured mesh. Unlike typical transition models that suffer from non-local calculations, by utilizing the vorticity Reynolds number ($Re_v = \frac{\mu y^2}{\rho} |\frac{\partial U}{\partial y}|$ where y is again the distance from the nearest wall), the $\gamma-Re_{\theta}$

transition model correlates the transition onset with the local boundary-layer quantities through empirical relations. Since Re_v can be calculated locally, this model has the advantage that can be easily implemented into RANS equations. It involves two transport equations for the intermittency, γ , and the transition onset momentum thickness Reynolds number, $\hat{Re}_{\theta t}$, as follows:

$$\frac{\partial(\rho\gamma)}{\partial t} + \nabla \cdot (\rho\gamma \mathbf{U}) = P_{\gamma} - E_{\gamma} + \nabla \cdot \left((\mu + \frac{\mu_t}{\sigma_f}) \nabla(\gamma) \right)$$
(1a)

$$\frac{\partial \left(\rho \hat{R} e_{\theta t}\right)}{\partial t} + \nabla \cdot (\rho \hat{R} e_{\theta t} \mathbf{U}) = P_{\theta t} + \nabla \cdot \left(\sigma_{\theta t} (\mu + \mu_t) \nabla (\hat{R} e_{\theta t})\right),\tag{1b}$$

where σ_f and $\sigma_{\theta t}$ are the model constants that are set to 1 and 2, respectively. The two source terms, P_{γ} and E_{γ} , in the right hand side of Eq. (1a) are responsible for the transition onset and destruction/relaminarization, respectively. The production term $P_{\theta t}$ in Eq. (1b) adjusts the value of the transition onset momentum thickness Reynolds number to match the value obtained from the empirical correlations (equations 35 and 36 in the paper by Langtry and Menter (2009)) outside the boundary layer, and vanishes inside the boundary layer. These transport equations are discretized with second order upwind method and calculated at each cell. The intermittency equation initiates the transition by affecting the turbulent kinetic energy (TKE) production downstream of the transition point. Aside from all the local calculations and correlations in the γ -equation to treat transition, the non-local events outside the boundary layer, such as free stream TKE decay and pressure gradient, impact the transition process by altering the turbulent intensity. In fact, these non-local effects form the basis of the empirical-based models of transition (Abu-Ghannam and Shaw, 1980). The momentum thickness Reynolds number, which is an important part of this model, is devised to handle these non-local effects on the transition

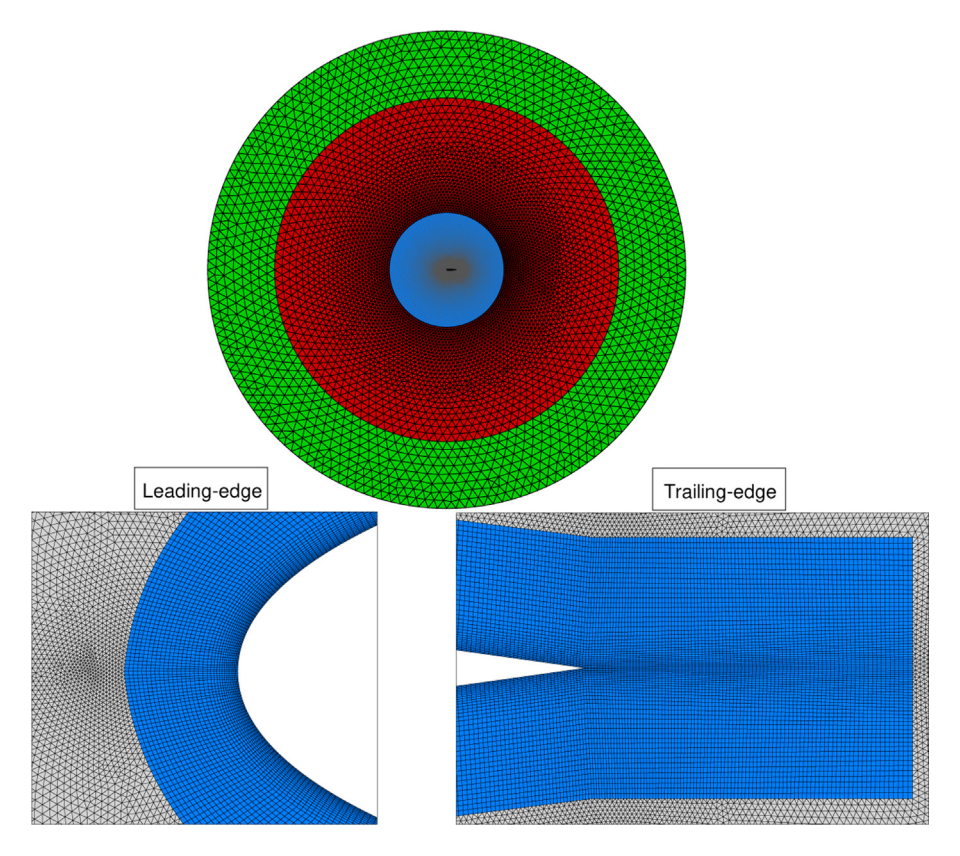


Fig. 1. Mesh topology in the farfield (top picture) and near the leading edge and trailing-edge (bottom pictures) of the airfoil. The blue region near the airfoil constitutes of high resolution structured grids that contains the boundary layer and the gray region is made of unstructured triangular elements. (For interpretation of the references to colour in this figure legend, the reader is referred to the web version of this article.)

onset by manipulating the source term in the intermittency equation. These equations interact with the $k - \omega$ SST model by modifying some of the source terms in the k- equation (Fluent, 2009), while the ω -equation remains intact.

The added transport equations require boundary conditions on the airfoil surface, inlet and outlet. On the no-slip wall (aifoil) and constant pressure outlet, zero normal flux condition is prescribed for γ and Re_{θ} . At the inlet station, γ is set to 1 and Re_{θ} is to be found from empirical correlations in the model based on the inlet turbulent intensity. These correlations are provided in equations 35 to 38 in Langtry and Menter (2009).

3. Validation

In order to validate the numerical setup, the experimental study by Kim and Chang (2014) for a pitching NACA 0012 at a transitional Reynolds number is selected. They provide experimental measurements for the lift history during the maneuver along with the pressure distribution and flow visualization at a few important instances. In particular, we select the experimental case of the Reynolds number $Re = 48 \times 10^3$ where transition occurs. In this case, the airfoil is hinged at the quarter-chord point with 6° pitching amplitude and reduced frequency of k = 0.1. The same geometry and conditions are used for the CFD validation. The free stream turbulent intensity is selected to be TI = 0.35% since TI is reported to be less than 0.4% in the experimental study.

Fig. 2 shows a good agreement between the lift history measurements of Kim and Chang (2014) and our computational simulation. The CFD results are provided at two different Reynolds numbers of $Re = 48 \times 10^3$ and $Re = 75 \times 10^3$. The reason for choosing the higher Reynolds number ($Re = 75 \times 10^3$) is that the SST transition model shows a dissipative behavior for $Re < 70 \times 10^3$ based on our numerical results. The ripples seen in Fig. 2 for the curve of $Re = 48 \times 10^3$ occur near the instants of maximum pitching velocity where the flow is more prone to separation (Taha and Rezaei, 2019). At these instants, the interaction between the laminar separation bubble and downstream adverse pressure gradient is significant, and the model is unable to find the correct transition point.

The discrepancy in the maximum lift coefficient may actually be attributed to the experimental results per se. The maximum lift coefficient in the experimental data is almost equal to the one obtained from thin airfoil theory: $2\pi(6^{\circ} \times \frac{\pi}{180}) = 0.66$, which is not expected because (i) an actual airfoil has a lift curve slope that is smaller than the

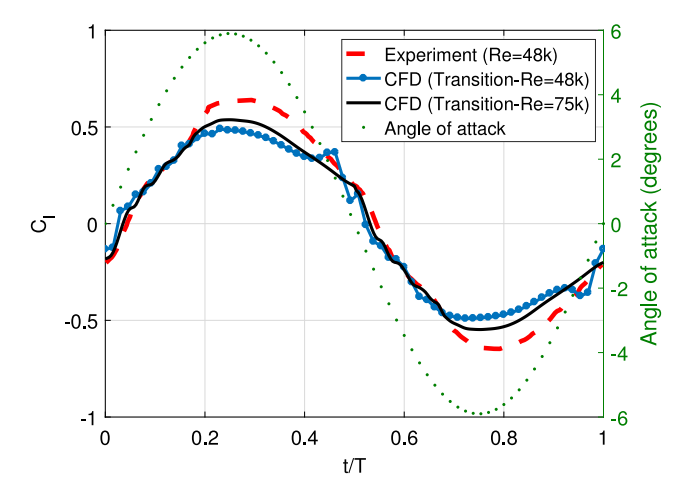


Fig. 2. Validation of the computational setup adopted from Rezaei and Taha (2019). Comparison between the lift history from CFD and the experimental study (Kim and Chang, 2014) for a pitching NACA 0012 with $\alpha(t) = 6^{\circ} \sin(\omega t)$ and k = 0.1 undergoing transition.

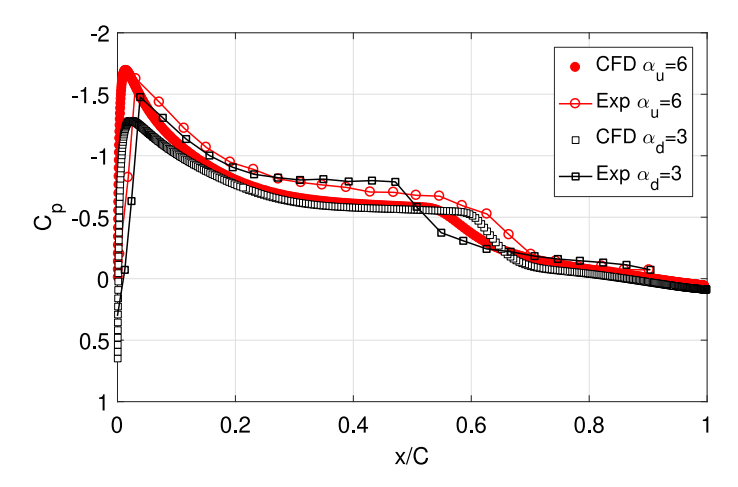


Fig. 3. Comparison of the pressure coefficient on the suction side of the pitching airfoil between the CFD and the experimental (exp) results (Kim and Chang, 2014) at one instance during upstroke ($\alpha_u = 6^\circ$) and one instance during downstroke($\alpha_d = 3^\circ$) for a pitching NACA 0012 with $\alpha(t) = 6^\circ \sin(\omega t)$ and k = 0.1 at $Re = 75 \times 10^3$.

theoretical value of 2π , and (ii) the amplitude of the unsteady lift must be attenuated due to wake effects: Theodorsen lift deficiency (Theodorsen and Mutchler, 1935).

To validate the local flow details and the transition point dynamics, we consider the pressure coefficient C_p at two important instances, i.e. one instance ($\alpha_u = 6^\circ$) in the upstroke near stroke reversal (highest pitching angle) and one instance ($\alpha_d = 3^\circ$) in the downstroke, as shown in Fig. 3. As described by Arena and Mueller (1980) and recently by Boutilier and Yarusevych (2012), the start of the short plateau in the mid-chord region corresponds to the laminar separation, followed by a sudden drop indicating the transition point. Then the pressure recovery region is attributed to turbulent reattachment. A good agreement is observed in terms of the magnitude of the pressure coefficient and transition point. The reason for slightly higher values of C_p in the experimental results compared to CFD is the same as the above explanation for C_l difference near the stroke reversal. The $\alpha_d = 3^\circ$ case corresponds to the instant where the airfoil is at the three-quarter of the downstroke motion where more complicated flow events are expected due to the interaction with the vortical region formed in the upstroke near the trailing-edge. Under this condition, the transition point obtained from the CFD results is delayed roughly 10 percent.

Furthermore, validation of the flow field near the trailing-edge of the foil at six different instances during the pitching cycle for the same case was done in our recent work (Rezaei and Taha, 2019), which showed a good agreement with the flow visualization from the experiment (Kim and Chang, 2014). In this manuscript, the streamlines for two of those instances are provided for completeness. As described by Kim and Chang (2014), a mushroom structure is observed near the trailing-edge when $\alpha_u = 3^{\circ}$ as shown in Fig. 4a. This structure is mitigated (i.e. the two vortices are separated) when a new vortex starts to form at the trailing edge when $\alpha_u = 3.9^{\circ}$ (Fig. 4b).

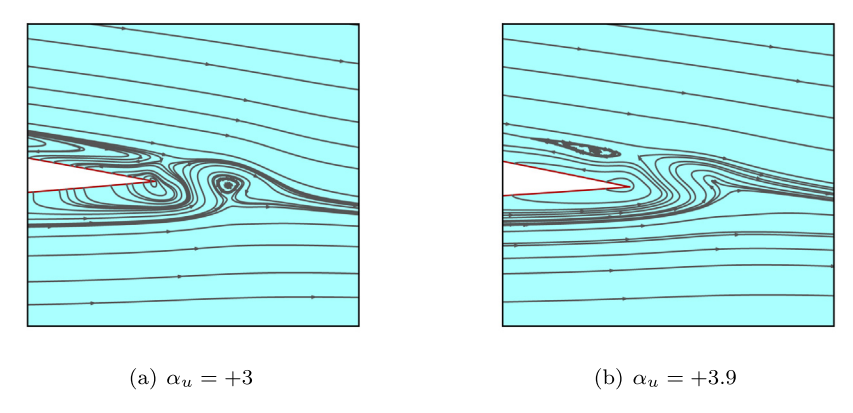


Fig. 4. Streamlines near the trailing-edge at two different instances during upstroke.

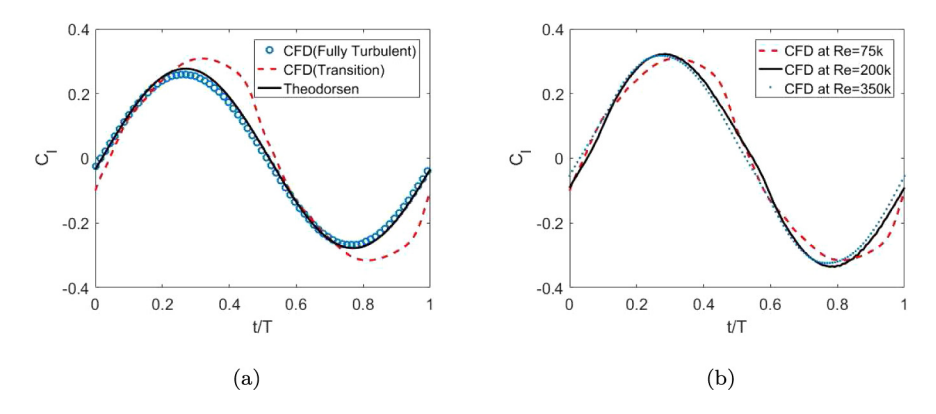


Fig. 5. Lift history of a pitching NACA 0012 with $\alpha(t) = 3^{\circ} \sin(\omega t)$ and k = 0.1 undergoing transition: (a) Comparison of the lift history between Theodorsen model and CFD results at $Re = 75 \times 10^3$ using transition and fully turbulent models and (b) Effect of Reynolds number on the lift history utilizing transition model in CFD.

4. Results

4.1. Effect of transition on the lift dynamics

CFD simulations have been carried out in the range of moderate Reynolds number, $Re = 75 \times 10^3 - 400 \times 10^3$ and motion reduced frequency k = 0.1 to investigate the effect of transition on the lift dynamics of a pitching airfoil at zero mean angle of attack with 3 degrees pitching amplitude. As shown in our preliminary analysis (Rezaei and Taha, 2019), it should be emphasized that in this regime, the effect of transition on the lift dynamics is significant. That is, if transition is not taken into account or properly modeled, the computed aerodynamic loads will be noticeably different. Based on Fig. 5a, assuming a fully turbulent flow without modeling the transition, using a simple harmonic motion as an input for the pitching airfoil (time-varying angle of attack) results in a harmonic lift response at the same frequency (i.e., linear dynamics). However, at the same Reynolds number, the same input results in a different lift dynamics when transition is considered. In fact, in the presence of transition, the dynamics of the flow is no longer linear as the output (lift) possesses higher harmonics compared to the single-harmonic input (angle of attack), which will be the focus of the coming sections. For better comparison, the Theodorsen results at k = 0.1 is also plotted, which matches the linear results of the fully turbulent case. To put in a nutshell, a fully turbulent flow results in a linear lift dynamics whereas laminar-to-turbulent transition induces non-linearity in the lift dynamics.

This criterion can be used as an indicator for transition. To further investigate this point, the effect of Reynolds number on the lift history is shown in Fig. 5b. It can be seen that increasing the Reynolds number makes the output signal (lift) to resemble more a pure sinusoid. It is found that, under the conditions used in this study, the lift dynamics becomes very close to the fully turbulent case for $Re > 400 \times 10^3$, and below this value, careful consideration is required to capture the transition, specifically when $Re < 200 \times 10^3$ where transition effects are significant.

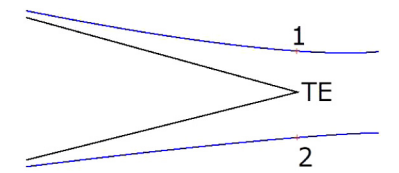


Fig. 6. A zoom at the trailing-edge and its boundary layer. The blue lines represent the edge of the boundary layers and the red dots (points 1 and 2) represent the edge of the boundary layers at the trailing-edge station.

4.2. Flow near the trailing-edge and the kutta condition

Potential flow theory is indeed a milestone in the history of aerodynamics, forming the basis of almost all the analytical theories in steady and unsteady aerodynamics. It states that for a thin airfoil subjected to small deflections at high Reynolds numbers, the flow can be assumed everywhere irrotational except for a thin layer around the airfoil (boundary layer) and in the wake (only appears in the unsteady theories). These regions are modeled with sheets of (or point) vortices whose strength is determined from the kinematic boundary condition on the airfoil (no-penetration). Laboring this algorithm, a unique solution cannot be determined unless the value of the circulation is known. Therewith the Kutta condition comes to play, which dictates vanishing circulation distribution at the trailing-edge (zero loading at the trailing-edge) based on physical observations from the flow field around the airfoil trailing-edge. This condition forms the bridge that connects potential flow to viscous flow and essentially relates the amount of generated vorticity flux in the boundary layer to the vorticity in the wake (Sears, 1976). In the potential flow framework, there are many representations of the Kutta condition; one dictates zero loading at the trailing-edge, which is stated as

$$\lim_{y \to 0^+} P(\text{TE}, y) = \lim_{y \to 0^-} P(\text{TE}, y),\tag{2}$$

where P(TE, y) represents the pressure at the trailing-edge (TE) station at a distance y above the trailing-edge point; that is the trailing-edge is approached from the top by taking the limits as $y \to 0^+$ and from the bottom as $y \to 0^-$. In the corresponding viscous flow accompanied by the boundary layer development on the top and bottom surfaces, this condition means equal pressure at the edges of the boundary layers on each side, which is indeed generally true. Nevertheless, under certain conditions such as low Reynolds number flows, high frequency motion of the airfoil and laminar-to-turbulent transition, deviation is observed from the classical Kutta condition (Taha and Rezaei, 2019). To elaborate more, consider the viscous flow around an airfoil and regard the flow near the trailing-edge, shown in Fig. 6. Since the potential flow pressure distribution over the thin airfoil represents the pressure distribution at the edge of the boundary layer in the viscous flow, Eq. (2) applied within the potential flow solver, yields $P_1 = P_2$ in the presence of boundary layers, where the points 1 and 2 lie on the edge of the boundary layer at the trailing-edge station (Fig. 6).

In our recent effort (Taha and Rezaei, 2019), we have shown while the main assumption underpinning Prandtl's boundary layer theory (pressure is constant along a direction perpendicular to the surface inside the boundary layer thickness) is valid over the majority of the airfoil length, it may not be valid in the immediate vicinity of the trailing-edge. The situation is exacerbated when laminar-to-turbulent transition occurs. That is, there may be a considerable pressure rise ΔP across the boundary layer. In this case, the physical condition (2) results implies

$$P_1 - \Delta P_1 = P_2 - \Delta P_2,\tag{3}$$

In addition, the unsteady Bernoulli's equation provides a relation between P_1 and P_2 (note that point 1 and 2 lie on the edge of the boundary layer) as:

$$\frac{P_1}{\rho} + \frac{1}{2}V_1^2 + \frac{\partial \phi_1}{\partial t} = \frac{P_2}{\rho} + \frac{1}{2}V_2^2 + \frac{\partial \phi_2}{\partial t},\tag{4}$$

where V is the potential flow velocity at the edge of the boundary layer and ϕ is the corresponding velocity potential. Recalling that the velocity potential ϕ due to a vortex Γ is given by $\phi = \frac{\Gamma}{2\pi}\theta$ and calculating the jump in ϕ along a closed contour (from $\theta = 0$ to $\theta = 2\pi$), one obtains $\phi_1 - \phi_2 = \Gamma$. Combining the later with Eqs. (3) and (4), we obtain

$$\dot{\Gamma} = \frac{1}{2} \left(V_2^2 - V_1^2 \right) + \frac{\Delta P_2 - \Delta P_1}{\rho},\tag{5}$$

To recover the common form of the Kutta condition typically applied in the classical theory of unsteady aerodynamics, we set $\Delta P_1 = \Delta P_2 = 0$ and $V_{1,2} = U \pm \frac{1}{2} \gamma_{\text{TE}}$. In this case, Eq. (5) results in

$$\dot{\Gamma}_{\text{Kutta}}(t) = -U_{\infty} \gamma_{\text{TE}}(t), \tag{6}$$

where γ_{TE} is the circulation distribution at the trailing-edge (instantaneous strength of the shed vortex sheet per unit length at the shedding time) calculated as

$$\gamma_{TE}(t) = V_2 - V_1,\tag{7}$$

Z-vorticity

LSB

(b)

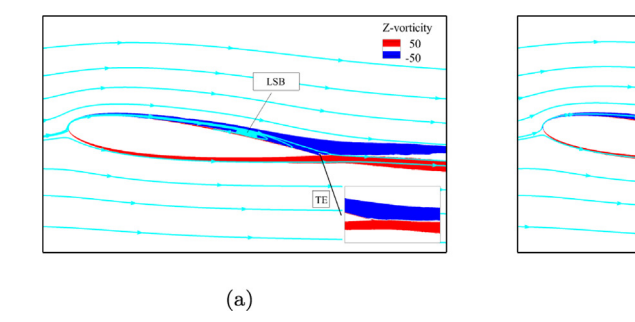


Fig. 7. Vorticity contours around a pitching NACA 0012 with $\alpha(t) = 6^{\circ} \sin(\omega t)$ and k = 0.1 and zoom-in near the trailing-edge at (a) $\alpha = \frac{A}{2}$, $\dot{\alpha} = \frac{\sqrt{3}}{2}Aw$ and (b) $\alpha_{max} = A$, $\dot{\alpha} = 0$.

Thus, the *exact* circulation dynamics governed by Eq. (5) reduces to the classical Kutta's circulation governed by Eq. (6) using two assumptions: Linearization of the first term (velocity-term) and neglecting the second term due to pressure differences across the boundary layers. The former assumption is quite accurate for small deflections (small α). In this work, we show that the transition effects on the lift dynamics are related to (can be captured by) the pressure term in the circulation dynamics Eq. (5).

Transition induces non-linearity in the lift dynamics. Since lift is ultimately dictated by the Kutta condition, one can legitimately deduce that the classical Kutta condition is violated, and special care is required to study the flow near the trailing-edge. It is worth noting that unlike the steady boundary layer where the flow reversal corresponds to zero shear stress at the wall (defining the separation phenomenon), in the unsteady case, zero shear stress (or flow reversal) is not an indication of boundary layer separation. In other words, the boundary layer assumptions may remain correct while flow reversal is observed inside it. In fact, separation might happen far downstream of the point of zero shear stress in unsteady flows (Sears and Telionis, 1975).

4.3. Persistence of the boundary layer in transition

Fig. 7 shows the vorticity contours and streamlines around the pitching NACA 0012 with 6 degrees pitching amplitude and motion reduced frequency of 0.1 ($A=6^\circ$ and k=0.1) at the highest geometric incident angle of the airfoil, $\alpha_u=6$, and at a position where both α and $\dot{\alpha}$ are significant. Note that in unsteady aerodynamics, $\dot{\alpha}$ affects the effective angle of attack defined as $\alpha_{eff}=\alpha_{3/4}=\alpha+\dot{\alpha}c/2U_\infty$ in this case of pitching around the quarter-chord point. It can be seen that the LSB is initially formed close to the trailing-edge (Fig. 7a) and is observed on the mid-upper surface at the highest geometric angle of attack (Fig. 7b). If the airfoil reaches higher angles of attack, the leading-edge separation comes to play. In these cases, the mid-chord LSB is affected by the massive separation and forms a significantly larger vortical region (see figure 7 in Lee and Gerontakos (2004)).

In contrast to the dynamic stall cases where a massive separation is observed on the airfoil, all the studied cases lie within pre-dynamic-stall conditions. As a results, the boundary layer behaves similar to that of attached flow in the sense that its edge is detectable all the way to the trailing-edge where the wake begins (Fig. 7). Furthermore, the zoom-in on the flow in the vicinity of the trailing-edge in both cases does not indicate any noticeable separation upstream of the trailing-edge. These findings are in accordance with the pressure coefficient results (Fig. 3); if significant separation had happened in the flow, the pressure distribution would have shown a flat trend in the separated region while Fig. 3 shows a monotonically decreasing pressure. Moreover, the pitching amplitude in the upcoming results is at most 3 degrees, which helps the flow even more to remain attached. Consequently, by using the vanishing vorticity criteria, the edge of the boundary layer can be determined at all the sections of the airfoil. To do this, the magnitude of the vorticity normalized by its maximum inside the boundary layer (which happens near the airfoil surface) is tracked normal to the surface. The edge of the boundary layer is detected when the normalized vorticity reaches 1 percent. Since the focus of this study is to investigate the Kutta condition, the edge of the boundary layers on the top and bottom surfaces at the trailing-edge station have been found. Then, the values of pressure and velocity at those locations have been extracted from the CFD results for further investigations provided in the coming sections.

4.4. Effect of transition on circulation dynamics

In the current study, the circulation dynamics is investigated at two different Reynolds numbers: $Re = 75 \times 10^3$ and $Re = 200 \times 10^3$; four different reduced frequencies: k = 0.05, 0.1, 0.2, 0.3; and three different pitching amplitudes: A = 0.5, 1.5 and 3 degrees. All the studied cases (9 in total) are shown in Table 1.

Before discussing the effect of each parameter on the circulation dynamics, let us point out some noteworthy findings. For simplicity purposes, let, $\dot{\Gamma}_U = \frac{1}{2} \left(V_2^2 - V_1^2 \right)$, $\dot{\Gamma}_P = (\Delta P_2 - \Delta P_1)/\rho$, $\dot{\Gamma}_{total} = \dot{\Gamma}_U + \dot{\Gamma}_P$. It is also interesting to compare with

Table 1The pitching amplitudes, motion reduced frequencies and Reynolds numbers of all the studied cases.

	Α	k			
		0.05	0.1	0.2	0.3
$Re = 75 \times 10^3$	0.5°		*		
	1.5°		*		
	3°	*	*	*	*
$Re = 200 \times 10^3$	0.5°		*		
	3°	*	*		

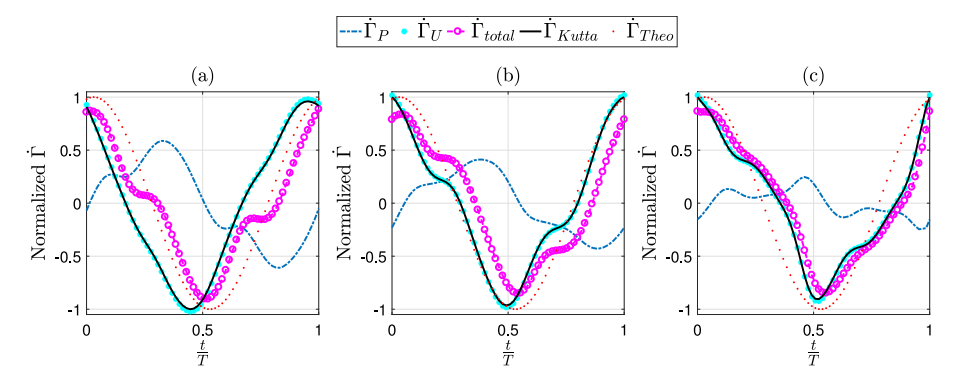


Fig. 8. $\dot{\Gamma}$ history at $Re = 7.5 \times 10^4$, k = 0.1, and three different pitching amplitudes A: (a) $A = 0.5^{\circ}$, (b) $A = 1.5^{\circ}$, and (c) $A = 3^{\circ}$.

Theodorsen's rate of change of circulation $\dot{\Gamma}_{Theo}$. For a pitching airfoil hinged at the quarter-chord point, the potential-flow frequency response of the bound circulation is given by $\Gamma_{Theo} = 2\pi \, \rho b C_{\Gamma}(k) [U_{\infty} \alpha + b \dot{\alpha}]$, where $C_{\Gamma}(k) = \frac{-2e^{-jk}}{jk\pi \left(H_1^{(2)}(k) + jH_0^{(2)}(k)\right)}$ is

the circulation transfer function in the frequency domain (Taha and Rezaei, 2020). Note that $H_n^{(m)}$ is the Hankel function of mth kind of order n. As discussed above, in potential flow theory, $\dot{\Gamma}_P$ should be zero assuming zero pressure rise across the boundary layer at the trailing-edge station (zero loading). This assumption is accurate for high Reynolds number steady flows or unsteady flows at low reduced frequencies (quasi-steady conditions). Nevertheless, under unsteady conditions undergoing transition, this assumption might not be accurate and needs further investigation. Figs. 8, 11 and 14 show the time-history of all the defined $\dot{\Gamma}$'s for all the studied cases. Note that all the results come from a pure sinusoidal pitching input, i.e. simple harmonic motion, and have been normalized by the maximum value of the $\dot{\Gamma}_{\text{Kutta}}$. Interestingly, Figs. 8, 11 and 14 indicate that $\dot{\Gamma}_{\text{Kutta}}$ and $\dot{\Gamma}_U$ coincide in all the cases reflecting the fact that the linearization is fairly accurate, which is expected because of the considered small amplitudes. Therefore, any non-linearity in the flow dynamics should not be attributed to geometric non-linearities due to large angles. Moreover, since $\dot{\Gamma}_U \approx \dot{\Gamma}_{\text{Kutta}}$, we have

$$\dot{\Gamma}_{U} = \dot{\Gamma}_{Kutta} \to \frac{1}{2} (V_2 + V_1) (V_2 - V_1) = U_{\infty} (V_2 - V_1)$$
(8)

resulting in $V_2 + V_1 = 2U_{\infty}$. So, the non-linear trend of the $\dot{\Gamma}_U$ must be attributed to the $V_2 - V_1$ term as $V_2 + V_1$ is shown to be equal to a constant (twice the free stream velocity).

In the upcoming sections, the results are provided in terms of rate of change of the circulation $\dot{\Gamma}$ coming from different sources and the Fast Fourier Transform (FFT) results of $\dot{\Gamma}_U$ and $\dot{\Gamma}_P$ to show both their linear–nonlinear behavior and their relative contribution to the total circulation. If the flow dynamics is purely linear, only the first harmonic would be expected; the emergence of a higher harmonic peak would certainly imply a nonlinear behavior. For example, a peak at the second (third) harmonic implies a quadratic (cubic) nonlinearity, and so on (Nayfeh and Mook, 2008; Nayfeh and Balachandran, 2008). Furthermore, the larger the higher-harmonic peak is relative to the first-harmonic one, the more significant the nonlinear contribution is. In order to elaborate more on the flow events near the TE, the history of the boundary layer thickness on the top and bottom of the airfoil have been plotted. All the figures were normalized by the maximum thickness of the boundary layer. Since the airfoil is symmetric and the motion is also symmetric, the top and bottom boundary layers at the trailing-edge reach to the same maximum thickness over the cycle. Therefore, both are normalized by the same value. The behavior of the boundary layer edge at the trailing-edge is an interesting result and can be correlated to the formation and movement of the LSB inside the boundary layer in the mid-chord region, which is not discussed in this paper and is provided for completeness.

4.4.1. Effect of pitching amplitude (A) on circulation dynamics

In this section, the effect of pitching amplitude (\mathring{A}) on the $\mathring{\Gamma}$'s is investigated while the two other parameters are kept constant at $Re = 7.5 \times 10^4$ and k = 0.1. Since the objective of this article is to focus on transition-induced non-linearity on

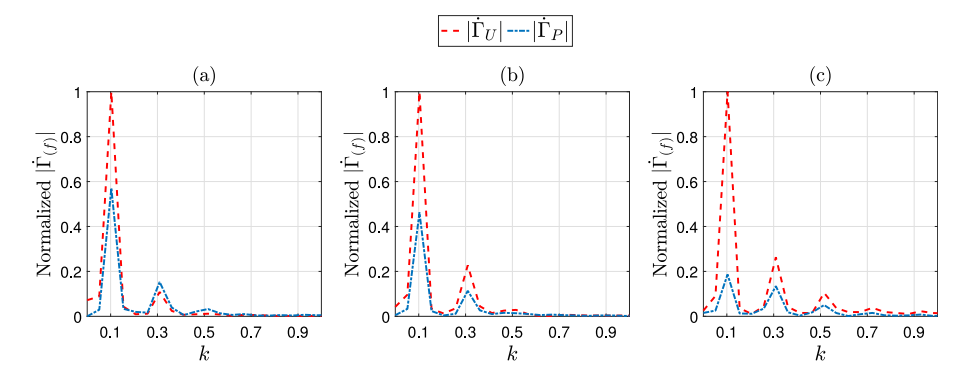


Fig. 9. FFT of $\dot{\Gamma}_{IJ}$ and $\dot{\Gamma}_{P}$ at $Re = 7.5 \times 10^4$, k = 0.1, three different pitching amplitudes A: (a) $A = 0.5^{\circ}$, (b) $A = 1.5^{\circ}$, and (c) $A = 3^{\circ}$.

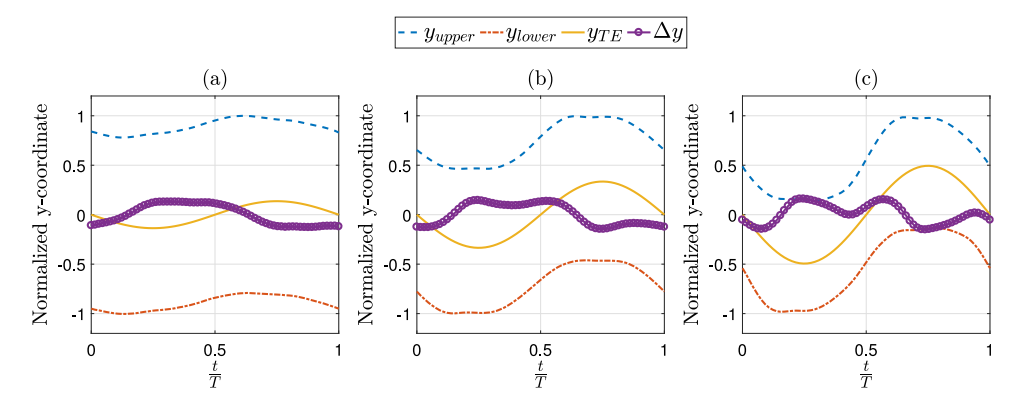


Fig. 10. Variation of the y-coordinate of the boundary layer at the top and bottom of the trailing-edge and the difference between them (in purple) at $Re = 7.5 \times 10^4$, k = 0.1, and three different pitching amplitudes A: (a) $A = 0.5^\circ$, (b) $A = 1.5^\circ$, and (c) $A = 3^\circ$. (For interpretation of the references to colour in this figure legend, the reader is referred to the web version of this article.)

the lift dynamics in the pre-stall regime, the selected pitching amplitudes are fairly low. At lower amplitudes of pitching (Fig. 8a), $\dot{\Gamma}_U$ behaves more linear compared to higher pitching amplitudes (Fig. 8b, c) where the non-linear trend is more apparent. This result can be confirmed by inspecting the FFT figures of $\dot{\Gamma}_U$ and $\dot{\Gamma}_P$ (Fig. 9). Interestingly, both $\dot{\Gamma}_U$ and $\dot{\Gamma}_P$ possess cubic non-linearities in their response even at the considered small amplitudes and low frequency; the strength of this cubic non-linearity (i.e. third harmonic) relative to the linear response (first harmonic) increases as A increases. Of particular importance is the remarkable contribution of the $\dot{\Gamma}_P$ to $\dot{\Gamma}_{\text{total}}$ in all the cases in this section (ranging between 15% to 35%).

Fig. 8 shows that $\dot{\Gamma}_P$ is out of phase with respect to $\dot{\Gamma}_U$, which upon addition, would decrease the rate of circulation development (i.e. $\dot{\Gamma}_{\text{total}}$), causing a lag in circulation dynamics and consequently in lift dynamics too. The significant deviation of $\dot{\Gamma}_{\text{total}}$ from the classical linear theory of Theodorsen at a very small amplitude (0.5°) and low frequency (k=0.1), shown in Fig. 8a, is remarkable, and may be solely attributed to transition effects. However, increasing A, decreases the contribution of $\dot{\Gamma}_P$ and brings the $\dot{\Gamma}_{total}$ closer to $\dot{\Gamma}_U$ which is also reflected in the magnitude of the FFT results in Fig. 9 showing diminution of $|\dot{\Gamma}_P|$ when A increases. Nevertheless, we must point out that even in these cases of relatively larger amplitudes (Fig. 8c), the effect of $\dot{\Gamma}_P$ is not negligible and the rate of circulation development is quite far from the linear theory of Theodorsen.

It must be noted that since the dynamics of $\dot{\Gamma}_P$ is non-linear, the superposition principle is not applicable and there must be coupling between the dynamics of the two-subsystems representing $\dot{\Gamma}_U$ and $\dot{\Gamma}_P$. For instance, assume the total circulation development is written as $\Gamma_{total} = a \Gamma + f(\gamma)$ where the first linear term represents the Kutta circulation ($\dot{\Gamma}_{Kutta} = \dot{\Gamma}_U$), and the second non-linear term represents the $\dot{\Gamma}_P$. If this latter contribution is neglected, the circulation dynamics would be purely linear resulting in the classical theory of unsteady aerodynamics. However, when the second term does not vanish, the superposition principle cannot be applied; the total circulation cannot be decomposed into two contributions, one coming from each sub-system. Moreover, since $\dot{\Gamma}_P$ induces non-linearity in the total circulation, the non-linearity will also be inherited in the linear term ($a \Gamma$). That is, $\dot{\Gamma}_P$ is the main source of non-linearity in the response of $\dot{\Gamma}_U$ which explains why the CFD prediction of $\dot{\Gamma}_{Kutta}$ deviates from Theodorsen's.

In order to elaborate more on the flow events near the TE, the history of the boundary layer thickness on the top and bottom of the airfoil have been plotted in Fig. 10. All the figures were normalized by the maximum thickness of the

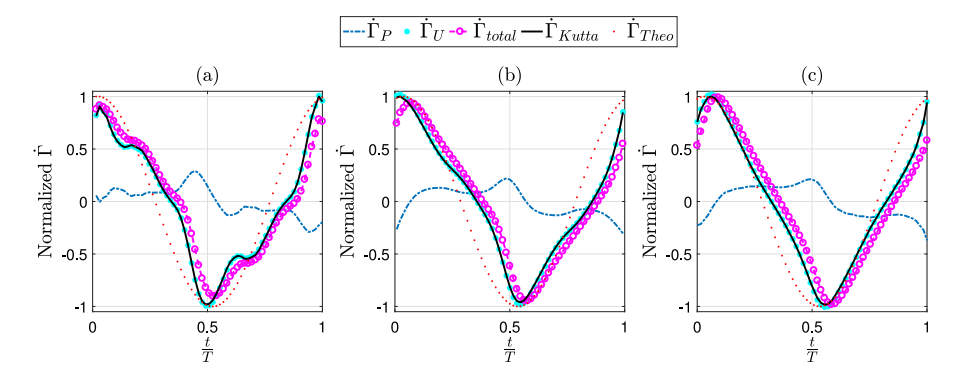


Fig. 11. $\dot{\Gamma}$ history at $Re = 7.5 \times 10^4$, $A = 3^\circ$ and three different motion reduced frequencies k: (a) k = 0.05, (b) k = 0.2, and (c) k = 0.3.

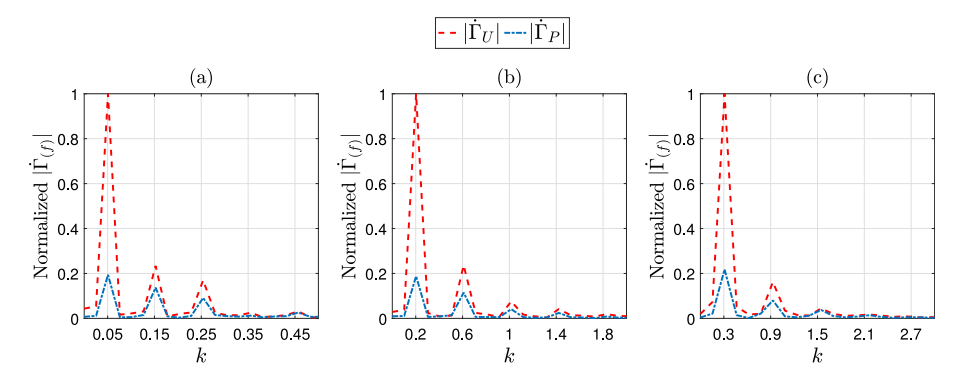


Fig. 12. FFT of $\dot{\Gamma}_U$ and $\dot{\Gamma}_P$ at $Re = 7.5 \times 10^4$, $A = 3^\circ$ and three different motion reduced frequencies k: (a) k = 0.05, (b) k = 0.2, and (c) k = 0.3.

boundary layer. Results reveal that the thickness of the boundary layer is not symmetric between the top and bottom surfaces of the airfoil otherwise, the Δy -plot would be flat zero. At lower A (Fig. 10a), the y_{upper} and y_{lower} are more sinusoidal while increasing the pitching amplitude excites more non-linearity in the system. (Fig. 10b,c)

4.4.2. Effect of reduced frequency (k) on circulation dynamics

The reduced frequency effect is analyzed by varying the pitching frequency and retaining the pitching amplitude and Reynolds number fixed at $A=3^\circ$ and $Re=7.5\times10^4$. Note that Figs. 8c, 9c, and 10c can also be considered in this section for comparison. Increasing k leads to an increase in the effective angle of attack causing the adverse pressure gradient effects to dominate the transition effects. Hence, $\dot{\Gamma}_U$ becomes more linear (Fig. 11), which can also be observed in the FFT results (Fig. 12). Because of the relatively large A, the $\dot{\Gamma}_P$ -contribution induces a small phase shift to $\dot{\Gamma}_{total}$ as discussed above. Even though there is a big difference between $\dot{\Gamma}_{total}$ coming from CFD and $\dot{\Gamma}_{Theodorsen}$; comparing the peaks imply that at low k values, Theodorsen phase matches with the numerical results, whereas at higher k values, a significant phase difference exists, which is similar to the viscous effects discussed by Taha and Rezaei (2019). The boundary layer thickness (Fig. 13) exhibits more sinusoidal trend as k increases which is in accordance with the circulation dynamics behavior.

4.4.3. Effect of Reynolds number (Re) on circulation dynamics

It is expected that increasing the Reynolds number will undermine the laminar-to-turbulent transition, therefore less non-linear behavior in the $\dot{\Gamma}$ -response. For this part, the numerical simulations were carried out at two different reduced frequencies and pitching amplitudes (refer to Table 1 for details). Considering Fig. 14a,b for the $\dot{\Gamma}$ -response when $A=3^\circ$ and comparing them with the ones for $Re=7.5\times10^4$ (Figs. 8c, 11a), a more linear trend in $\dot{\Gamma}_U$ is observed (can also be confirmed with the FFT results). Unlike the lower Reynolds number case where $\dot{\Gamma}_P$ shifted the $\dot{\Gamma}_{\rm total}$ to the right (i.e. induced a phase lag), at higher Reynolds number, this effect is not observed; $\dot{\Gamma}_{\rm total}$ follows $\dot{\Gamma}_U$ in phase. However, at both Reynolds numbers, $\dot{\Gamma}_P$ leads to an attenuation of the amplitude of $\dot{\Gamma}_{\rm total}$. The boundary layer thickness plots (Fig. 16a, b) also indicate smoother (akin to pure sinusoidal) trend of the flow.

Analogous to the influence of the pitching amplitude at the lower Reynolds number case (Fig. 8), it can be seen that at lower pitching amplitudes (Fig. 14c), $\dot{\Gamma}_P$ plays a considerable role in the dynamics of circulation. Nevertheless, it is interesting to point out that $\dot{\Gamma}_P$ possesses a linear behavior at small amplitude ($A = 0.5^{\circ}$), low frequency (k = 0.1), and high Reynolds number ($Re = 20 \times 10^4$), as shown in Fig. 14c which are the main assumptions underpinning the classical linear theory (see Fig. 15).

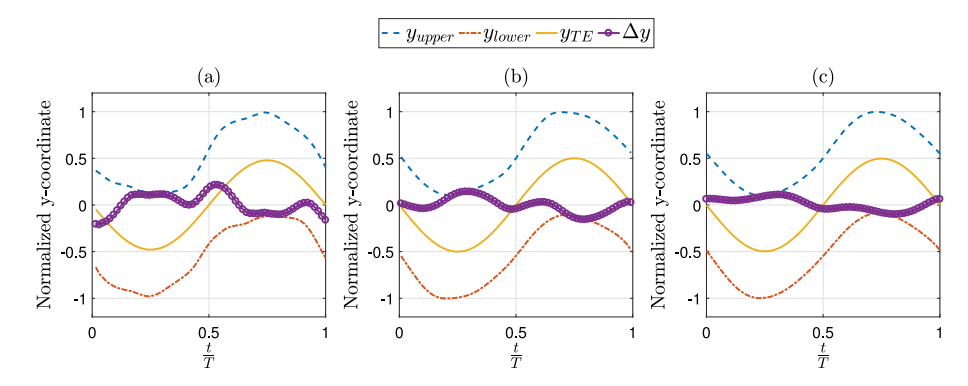


Fig. 13. Variation of the y-coordinate of the boundary layer at the top and bottom of the trailing-edge and the difference between them (in purple) at $Re = 7.5 \times 10^4$, k = 0.1, and three different pitching amplitudes A: (a) $A = 0.5^\circ$, (b) $A = 1.5^\circ$, and (c) $A = 3^\circ$. (For interpretation of the references to colour in this figure legend, the reader is referred to the web version of this article.)

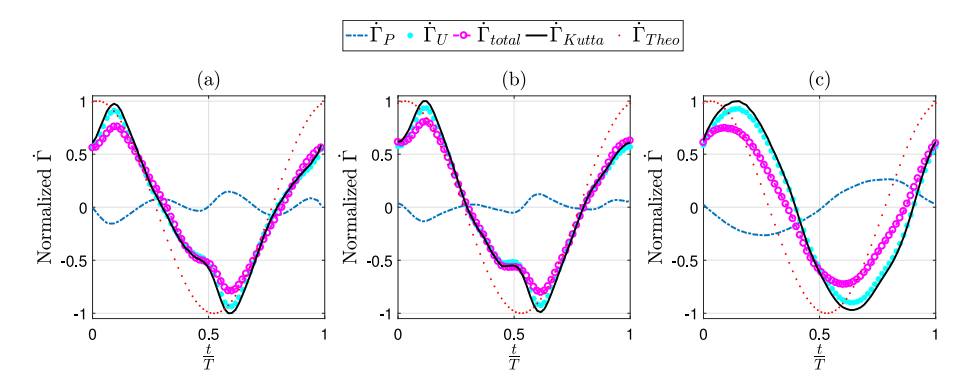


Fig. 14. $\dot{\Gamma}$ history at $Re = 20 \times 10^4$ when (a) k = 0.05 and $A = 3^{\circ}$, (b) k = 0.1 and $A = 3^{\circ}$, and (c) k = 0.1 and $A = 0.5^{\circ}$.

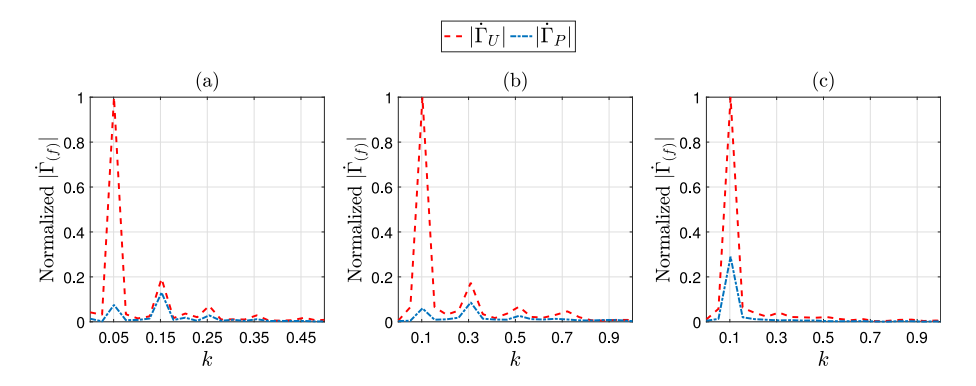


Fig. 15. FFT of $\dot{\Gamma}_U$ and $\dot{\Gamma}_P$ at $Re = 20 \times 10^4$ when (a) k = 0.05 and $A = 3^\circ$, (b) k = 0.1 and $A = 3^\circ$, and (c) k = 0.1 and $A = 0.5^\circ$.

5. Conclusion

CFD simulations (Reynolds-Averaged Navier–Stokes) are implemented to study the effects of the Laminar-to-Turbulent transition on the unsteady aerodynamic response of a pitching NACA 0012 airfoil. The $\gamma-Re_\theta$ transition model is coupled with $k-\omega$ SST turbulence model to account for transition effects. The numerical model (flow solver, closure model, dynamic mesh, etc.) is validated against an experimental study at a moderate Reynolds number of $Re=48\times10^3$, which shows the satisfactory accuracy of the numerical model. It has been shown that under the studied conditions (the airfoil, free stream turbulent intensity and reduced frequency), below $Re\approx200\times10^3$, transition has a significant effect on the lift response. It induces non-linearities in the lift and circulation dynamics, which diminish as Reynolds number increases toward the fully turbulent flow.

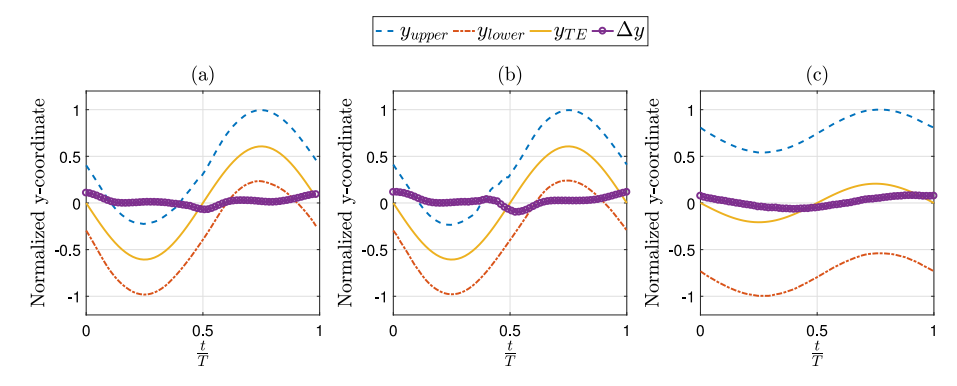


Fig. 16. Variation of the y-coordinate of the boundary layer at the top and bottom of the trailing-edge and the difference between them (in purple) at $Re = 7.5 \times 10^4$, k = 0.1, and three different pitching amplitudes A: (a) $A = 0.5^\circ$, (b) $A = 1.5^\circ$, and (c) $A = 3^\circ$. (For interpretation of the references to colour in this figure legend, the reader is referred to the web version of this article.)

Dissecting the flow field near the trailing-edge, we show that the Kutta condition is violated when transition occurs even at small pitching amplitudes ($A=0.5^{\circ}$) and low reduced frequencies (k=0.1); the rate of vorticity pumped into the wake from the boundary layer is quite different from the linear potential flow theory (e.g., Theodorsen). Consequently, the development of the bound circulation over the airfoil is quite different from the linear theory, and in fact possesses a non-linear behavior even at very small angles of attack and oscillation frequencies. We show that this deviation is due to a pressure jump across the boundary layer, which is caused by transition effects. Such a pressure jump is typically ignored in potential flow analysis. It leads to an additional contribution to the rate of change of bound circulation, which is found to be out of phase with respect to the main linear component. Hence, upon addition, it decreases the rate of change of bound circulation, causing a lag in circulation development and consequently in lift dynamics.

The effect of three parameters (pitching amplitude, frequency and Reynolds number) on the circulation dynamics is investigated. As pitching amplitude or frequency increases, the effects due to adverse pressure gradient dominate over the transition effects, diminishing the contribution of the pressure jump, leading to a more linear response. Also, increasing the Reynolds number, the flow becomes closer to a fully turbulent one where the linear response is dominant.

It is important to note that the above results can be exploited to extend the potential flow models to account for transition effects. This extension can be achieved by constructing a neural network model (or other approaches) of the static nonlinear function $\dot{\Gamma}=f(\Gamma;Re)$. The premise is that this functional dependence is independent of the motion kinematics. Thus, performing numerous high-fidelity (e.g., LES or DES) simulations at different amplitudes, frequencies, and Reynolds numbers, one can construct a static nonlinear map between the inputs (the total circulation Γ over the airfoil and the Reynolds number) and the output $\dot{\Gamma}$. Then, there may be several ways to extend potential-flow models to account for transition effects. For example, one may add a time-varying vortex Γ , coming from the neural network model, at the center of the cylinder domain, similar to Von Karman and Sears Kutta's vortex (von Karman and Sears, 1938). Alternatively, following Hemati et al. (2014), one may work in the cylinder domain istead of applying the Kutta condition ($\dot{\Gamma} = \dot{\Gamma}_{Kutta}$) at the trailing edge, a modified Kutta condition in the form ($\dot{\Gamma}_{modified} = \dot{\Gamma}_{Kutta} + \dot{\Gamma}$) is utilized, where the additional term Γ comes from the neural network model. Also, a third (perhaps simpler) approach is conceived by realizing that the quasi-steady circulation is the main input to potential-flow lift dynamics (Taha et al., 2014). Then, one may solve the lift dynamics (e.g., Theodorsen) due to a modified quasi-steady circulation $\Gamma_{QS} - \Gamma$.

CRediT authorship contribution statement

Amir S. Rezaei: Conceptualization, Methodology, Software, Validation, Formal analysis, Investigation, Resources, Data curation, Writing - original draft, Writing - review & editing, Visualization. **Haithem Taha:** Writing - review & editing, Visualization, Supervision, Project administration, Funding acquisition.

Declaration of competing interest

The authors declare that they have no known competing financial interests or personal relationships that could have appeared to influence the work reported in this paper.

Acknowledgments

The authors would like to acknowledge the support of the National Science Foundation, USA grant CBET-2005541.

References

Abu-Ghannam, B., Shaw, R., 1980. Natural transition of boundary layers—the effects of turbulence, pressure gradient, and flow history. J. Mech. Eng. Sci. 22 (5), 213–228.

Arena, A., Mueller, T., 1980. Laminar separation, transition, and turbulent reattachment near the leading edge of airfoils. AIAA J. 18 (7), 747-753.

Benton, S., Visbal, M., 2019. The onset of dynamic stall at a high, transitional reynolds number. J. Fluid Mech. 861, 860-885.

Boutilier, M.S., Yarusevych, S., 2012. Separated shear layer transition over an airfoil at a low reynolds number. Phys. Fluids 24 (8), 084105.

Darakananda, D., Eldredge, J.D., 2019. A versatile taxonomy of low-dimensional vortex models for unsteady aerodynamics. J. Fluid Mech. 858, 917–948. Deparday, J., Mulleners, K., 2019. Modeling the interplay between the shear layer and leading edge suction during dynamic stall. Phys. Fluids 31 (10), 107104.

Dovgal, A., Kozlov, V., Michalke, A., 1994. Laminar boundary layer separation: instability and associated phenomena. Prog. Aerosp. Sci. 30 (1), 61–94. Elsadek, A., Taha, H.E., El-Bayoumi, G.M., 2017. Stability analysis of longitudinal dynamics of hovering flapping mavs/insects. In: AIAA Atmospheric Flight Mechanics Conference. p. 1635.

Fluent, A., 2009. 12.0 User's Guide. Ansys Inc.

Gharali, K., Johnson, D.A., 2013. Dynamic stall simulation of a pitching airfoil under unsteady freestream velocity. J. Fluids Struct. 42, 228-244.

Greer, D., Hamory, P., Edwards, C., Krake, K., Drela, M., 2000. Design and predictions for high-altitude (low reynolds number) aerodynamic flight experiment. J. Aircr. 37 (4), 684–689.

Gupta, R., Ansell, P.J., 2018. Unsteady flow physics of airfoil dynamic stall. AIAA J. 57 (1), 165-175.

Hemati, M.S., Eldredge, J.D., Speyer, J.L., 2014. Improving vortex models via optimal control theory. J. Fluids Struct. 49, 91-111.

von Karman, T.H., Sears, W.R., 1938. Airfoil theory for non-uniform motion. J. Aeronaut. Sci. 5 (10), 379-390.

Kim, D.-H., Chang, J.-W., 2014. Low-reynolds-number effect on the aerodynamic characteristics of a pitching naca0012 airfoil. Aerosp. Sci. Technol. 32 (1), 162–168.

Langtry, R.B., Menter, F.R., 2009. Correlation-based transition modeling for unstructured parallelized computational fluid dynamics codes. AIAA J. 47 (12), 2894–2906.

Lee, T., Gerontakos, P., 2004. Investigation of flow over an oscillating airfoil. J. Fluid Mech. 512, 313-341.

Liu, J., Xiao, Z., Fu, S., 2018. Unsteady transition studies over a pitching airfoil using ak-ω-γ transition model. AIAA J. 1-6.

Lorber, P.F., Carta, F.O., 1994. Incipient torsional stall flutter aerodynamic experiments on three-dimensional wings. J. Propul. Power 10 (2), 217–224. McCroskey. W., Puccif. S., 1982. Viscous-inviscid interaction on oscillating airfoils in subsonic flow. AIAA J. 20 (2), 167–174.

McMasters, J., Henderson, M., 1980. Low-speed single-element airfoil synthesis. Tech. Soar. 6 (2), 1-21.

Menter, F.R., Langtry, R.B., Likki, S., Suzen, Y., Huang, P., Völker, S., 2006. A correlation-based transition model using local variables—Part i: model formulation. J. Turbomach. 128 (3), 413–422.

Mueller, T.J., DeLaurier, J.D., 2003. Aerodynamics of small vehicles. Annu. Rev. Fluid Mech. 35 (1), 89-111.

Nayfeh, A.H., Balachandran, B., 2008. Applied Nonlinear Dynamics: Analytical, Computational, and Experimental Methods. John Wiley & Sons.

Nayfeh, A.H., Mook, D.T., 2008. Nonlinear Oscillations. John Wiley & Sons.

Negi, P.S., Vinuesa, R., Hanifi, A., Schlatter, P., Henningson, D.S., 2018. Unsteady aerodynamic effects in small-amplitude pitch oscillations of an airfoil. Int. J. Heat Fluid Flow 71, 378–391.

Pelletier, A., Mueller, T.J., 2000. Low reynolds number aerodynamics of low-aspect-ratio, thin/flat/cambered-plate wings. J. Aircr. 37 (5), 825–832. Poirel, D., Mendes, F., 2014. Experimental small-amplitude self-sustained pitch-heave oscillations at transitional reynolds numbers. AIAA J. 52 (8), 1581–1590.

Raffel, M., Merz, C.B., Schwermer, T., Richter, K., 2015. Differential infrared thermography for boundary layer transition detection on pitching rotor blade models. Exp. Fluids 56 (2), 30.

Rezaei, A.S., Taha, H.E., 2019. Transition regime and its effects on the unsteady aerodynamic characteristics of a pitching airfoil. In: AIAA Scitech 2019 Forum. p. 0302.

Sears, W., 1976. Unsteady motion of airfoils with boundary-layer separation. AIAA J. 14 (2), 216-220.

Sears, W., Telionis, D., 1975. Boundary-layer separation in unsteady flow. SIAM J. Appl. Math. 28 (1), 215-235.

Smith, F., 1986. Steady and unsteady boundary-layer separation. Annu. Rev. Fluid Mech. 18 (1), 197-220.

Taha, H.E., Hajj, M.R., Beran, P.S., 2014. State-space representation of the unsteady aerodynamics of flapping flight. Aerosp. Sci. Technol. 34, 1–11. Taha, H.E., Rezaei, A.S., 2018. Unsteady viscous lift frequency response using the triple deck theory. In: 2018 AIAA Aerospace Sciences Meeting. p. 0038.

Taha, H., Rezaei, A.S., 2019. Viscous extension of potential-flow unsteady aerodynamics: the lift frequency response problem. J. Fluid Mech. 868, 141–175. http://dx.doi.org/10.1017/jfm.2019.159.

Taha, H.E., Rezaei, A.S., 2020. On the high-frequency response of unsteady lift and circulation: A dynamical systems perspective. J. Fluids Struct. 93, 102868.

Theodorsen, T., Mutchler, W., 1935. General Theory of Aerodynamic Instability and the Mechanism of Flutter. National Advisory Committee for Aeronautics Washington, DC.

Wagner, H., 1925. Über die Entstehung des dynamischen Auftriebes von Tragflügeln. ZAMM-J. Appl. Math. Mech./Z. Angew. Math. Mech. 5 (1), 17–35. Wang, S., Ingham, D.B., Ma, L., Pourkashanian, M., Tao, Z., 2010. Numerical investigations on dynamic stall of low reynolds number flow around oscillating airfoils. Comput. & Fluids 39 (9), 1529–1541.